RSC Advances

ROYAL SOCIETY OF CHEMISTRY

www.rsc.org/advances

Journal Name

ARTICLE

Direct Epitaxial CVD Synthesis of Tungsten Disulfide on Epitaxial and CVD Graphene

Received 00th January 20xx,
Accepted 00th January 20xx

DOI: 10.1039/x0xx00000x

www.rsc.org/

G. V. Bianco,[a†] M. Losurdo,[a] M. M. Giangregorio,[a] A. Sacchetti,[a]

P. Prete,[b] N. Lovergine,[c] P. Capezzuto,[a] and G. Bruno[a]

The direct chemical vapor deposition of WS_2 by $W(CO)_6$ and elemental sulfur as precursors onto epitaxial-graphene on SiC and CVD-graphene transferred on SiO_2/Si substrate is presented. This methodology allows the epitaxial growth of continuous WS_2 film with homogeneous and narrow photoluminescence peak without inducing stress or structural defects in the graphene substrates. The control of the WS_2 growth dynamics for providing the localized sulfide deposition by tuning the surface energy of the graphene substrates is also demonstrated. This growth methodology opens the way towards the direct bottom up fabrication of devices based on TMDCs/graphene van der Waals heterostructures.

Introduction

Whereas the "hype" on graphene seems to be weakening, a renewed interest in families of different layered materials such as dichalcogenides (e.g., MoS_2, and WS_2), nitrides (e.g., h-BN), and even oxides (e.g., TiO_2) is emerging.[1-4] Indeed, the quality of graphene continues to improve and its integration into heterostructures with other 2D materials represents an attractive technological perspective.[3] In particular, monolayers of transition metal dichalcogenides (TMDCs) such as MoS_2 and WS_2 have recently caught great interest as materials with properties complementary to those of graphene. In contrast to graphene, whose zero energy gap represents a limit for applications in logic electronics and field-effect transistors, monolayers of MoS_2 and WS_2 are semiconductors with a direct gap in the visible and, consequently, with a strong photoluminescence.[5-10] Therefore, their combination into heterostructures held together by van der Waals interactions (often referred as "van der Waals heterostructures") provides a great potential for the development of 2D electronic and optoelectronic devices.[3, 11-14]

Currently, many physical and chemical methodologies[15-28] are employed to prepare TMDCs and, among these, the direct growth of TMDC on other bidimensional materials represents a promising approach for the fabrication of van der Walls heterostructures.[27-31] This approach can provide cleaner and more defined interfaces if compared to the staking of 2D materials by transfer methods which often result in impurities trapped at the heterojunction interface.[20, 32] In fact, the interface quality has a fundamental role in defining the properties of TDMCs as well as of atomic-layered materials in general since substrate roughness and charged impurities can act as scattering centers strongly affecting their transport and optical properties. The important role of the interface quality on the properties of a TMDC has been highlighted by Okada et al. for the deposition of WS_2 on hexagonal boron nitride (h-BN).[27] They demonstrated an intense and narrow (fwhm of 26 meV) photoluminescence (PL) emission peak for WS_2 when deposited on an hexagonal and atomically flat surface. Similar results have been reported by Kobayashi et al. for the growth of WS_2 on graphite where micrometer WS_2 2D crystals presented a narrower PL peak rather than that shown by WS_2 grown on Al_2O_3 or SiO_2/Si.[33] Such PL responses are indicative of an improved structural quality that derives from the absence of dangling bonds on h-BN or graphite surfaces as well as on the face of a TMDCs layer which allows the WS_2 growth by Van der Waals epitaxy: the two van der Waals surfaces facing each other result in a heterostructure with an atomic order thickness and a very abrupt interface by drastically relaxing the lattice matching condition between the two materials.[34] Nevertheless, although van der Waals epitaxy has been demonstrated effective for providing micrometer-sized WS_2 crystals with high structural quality, TMDCs applications into van der Waals heterostructures need the controlled growth of layered materials as continuous film with homogeneous optical properties.

[a] *Institute of Nanotechnology, CNR-NANOTEC, Department of Chemistry, University of Bari, via Orabona 4, 70126 Bari, Italy.*
[b] *Institute for Microelectronic and Microsystems, National Research Council, UOS Lecce, Via Monteroni, I-73100 Lecce, Italy*
[c] *Department of Innovation Engineering, University of Salento, Via Monteroni, I-73100 Lecce, Italy.*
† email: giuseppevalerio.bianco@cnr.it

Electronic Supplementary Information (ESI) available: SEM image of epi-G on SiC substrate; Raman and PL mapping of WS_2 film. See DOI: 10.1039/x0xx00000x

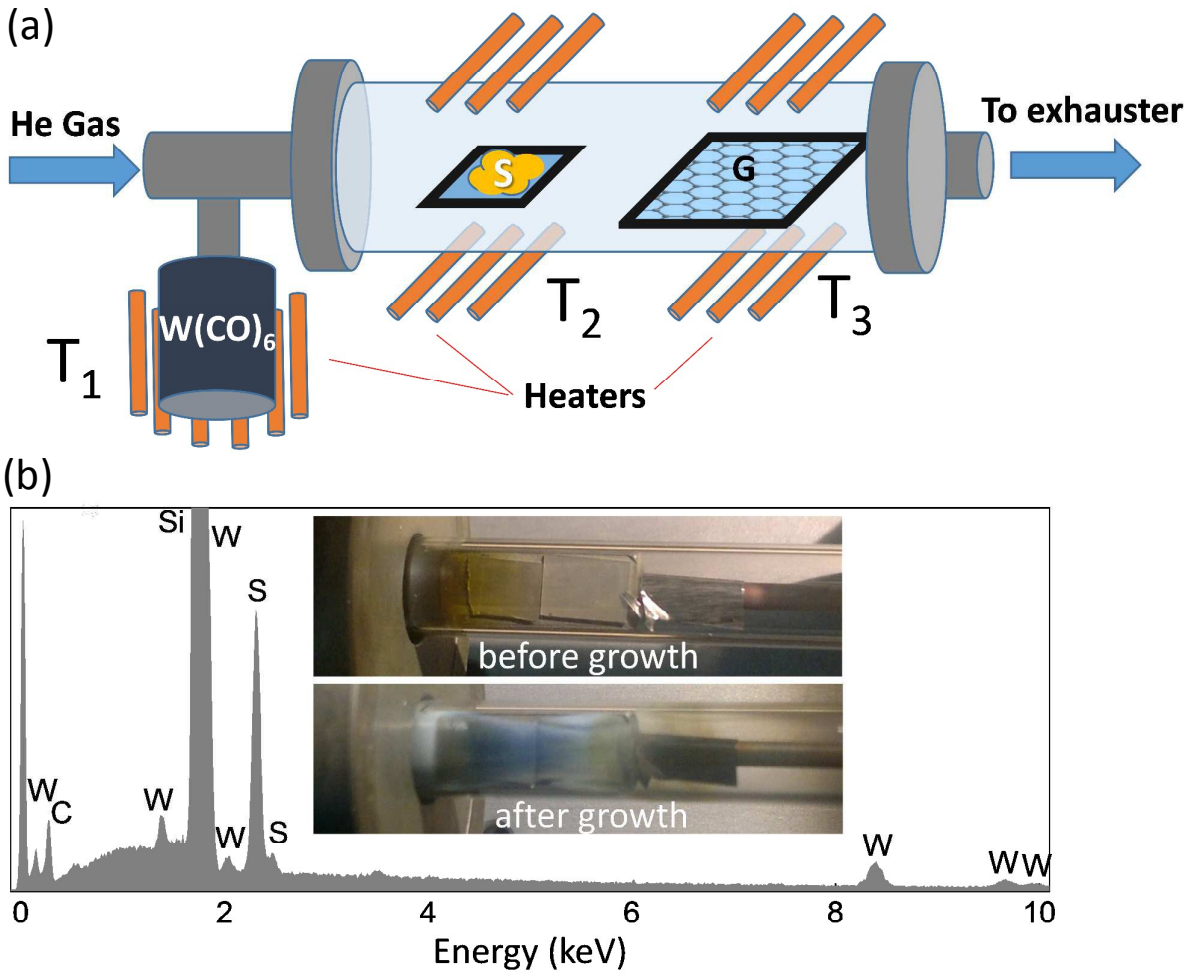

Fig. 1 (a) Schematic illustration of the CVD system used for the growth of WS_2. (b) EDS spectrum of synthesized WS_2 on epi-G/SiC. Photos of epi-G/SiC substrates in the quartz tube reactor before and after WS_2 growth are reported in the inset of b.

In this contribution, we report on the direct growth of WS_2 onto both epitaxial graphene (epi-G) and CVD graphene (CVD-G). To the best of our knowledge, this is the first study that shows how to deposit atomic layers of WS_2 by using elemental sulfur (S) and tungsten hexacarbonyl ($W(CO)_6$) as precursors. If compared with the commonly used WO_3 powder,[21, 33] such metal organic W precursor can provide a more precise control over the gas-phase chemistry for deposition on large area (as previously demonstrated for the WSe_2 growth).[29, 35] Moreover, the WS_2 deposition by direct reaction of gaseous precursors on the substrate surface, rather than by substrate metallization and subsequent sulfidization,[10,17] offers important advantages in terms of process scalability. We also demonstrate the flexibility of this new chemistry for providing the controlled WS_2 growth from isolated triangular crystals, to continuous few layer films, up to quasi-unidimensional nanostructures. The photoluminescence responses of deposited WS_2 films as function of their morphologies are investigated. Moreover, SEM analysis is performed for defining the WS_2 growth dynamic in order to achieve the controlled, also localized, WS_2 growth with homogenous thickness, and hence, optical properties

Results and discussion

The WS_2 film growth is carried out by the thermal decomposition of $W(CO)_6$ in presence of sulfur vapor according to the following reaction:

$$W(CO)_6 + S_2 \rightarrow WS_2 + {}_6CO \quad (1)$$

The scheme of the CVD system used for the growth of WS_2 is reported in fig. 1a. The quartz reaction tube for thermal CVD has two heated zones for the sulfur-powder boat and for the growth susceptor where the graphene substrate is loaded. After evaporation of the solid tungsten precursor ($W(CO)_6$) at 50°C (T_1), the last is mixed with helium carrier gas and passes through the quartz tube system where the small capsule with elemental sulfur is heated at 170°C (T_2). Then, the S_2 vapor is also mixed to the gas flow that reaches the graphene substrate heated at 600°C (T_3).

When epi-G/SiC is used as substrate, the WS_2 growth is evidenced by the colour changes of the transparent sample

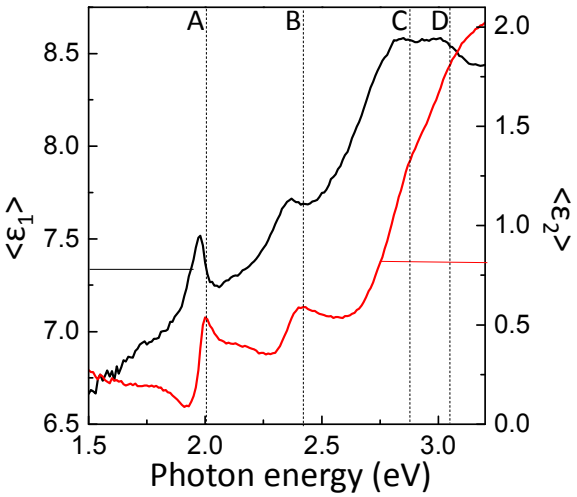

Fig. 2 SE spectra of the real (ε_1) and imaginary (ε_2) parts of the pseudodielectric function ($\varepsilon=<\varepsilon_1>+i<\varepsilon_2>$) of WS_2 grown on epi-G/SiC (deposition time of 10 min).

which becomes grey/blue in colour (insets of fig. 1b), and it is confirmed by the elemental composition obtained from the EDS-SEM microanalysis (fig. 1b).

Fig. 2 reports the real ($<\varepsilon_1>$) and imaginary parts ($<\varepsilon_2>$) of the pseudodielectric function of WS_2 grown on epi-G/SiC. Being the epi-G/SiC substrate almost transparent in the energy range from 1.5 to 3.2 eV, the pseudodielectric function ($<\varepsilon>=<\varepsilon_1>+i<\varepsilon_2>$) of the TMDC/graphene based heterostructures is dominated by the WS_2 contribution and the energies of the A, B, C, and D absorption peaks of WS_2 can be easily evidenced:[36, 37] A and B (around 2.00 and 2.45 eV, respectively) correspond to the excitonic transitions at the K point between the split valence band and the conduction band; C (≈2.85 eV) and D (≈3.11 eV) are associated with transitions away from the K point and between high density of states regions. The energies of these transitions are affected by interlayer interactions and show a consistent blue shift with decreasing layer numbers. In particular, a C transition located above 2.75 eV has been typically correlated to WS_2 monolayer.[9, 37]

The achieved WS_2 growth can be also attested by the comparison between Raman spectra of epitaxial graphene on SiC before and after the deposition process (fig. 3). In the range 1200–2000 cm^{-1}, the spectra present the Raman peaks of the SiC substrate overlapping the characteristic D and G peaks of graphene (approximately at 1350 and 1590 cm^{-1}, respectively). Conversely, the graphene 2D is clearly visualized at 2733 cm^{-1}. This peak can be fitted to a single Lorentzian (see the inset in figure 3) indicating the monolayer nature of the sample.[38] The WS_2 growth is inferred by a slight attenuation of the SiC Raman features and of the graphene 2D peak as well as by the appearance of the two WS_2 characteristic peaks at 355 and 417 cm^{-1}. The former is E^1_{2g} mode, which involves the in-plane displacement of W and S atoms, and the latter is the A_{1g} mode, which involves the out-of-plane displacement of S atoms.[39] The decrease in intensity of the SiC and graphene Raman features is attributed to interference effects and absorption of WS_2.[32] Noteworthy, the spectrum shape does not change (except for the signal attenuation) in the region around 1350 cm^{-1} where the graphene D peak is expected. This demonstrates that the growth process does not affect the graphene structural quality, since the occurrence of any damaging would increase the intensity of the D peak.

Raman analysis can also be used to identify and quantify the interfacial strain on the fabricated TMDC/G heterostructures.[32] The following equation correlates the graphene strain (ε) induced by the WS_2 deposition to the shift in wavenumber of the 2D Raman mode ($\omega-\omega_0$, where ω_0 is the initial wavenumber):

$$\varepsilon=(\omega-\omega_0)/2\gamma\omega_0 \quad (2)$$

where γ is the Gruneisen parameter, which uniquely depends on the material. Considering a 2D shift of 3 cm^{-1}, an initial position of 2733 cm^{-1}, and γ_{2D} of 2.6,[32] we have estimated a negligible compressive strain of about 0.02%. This result

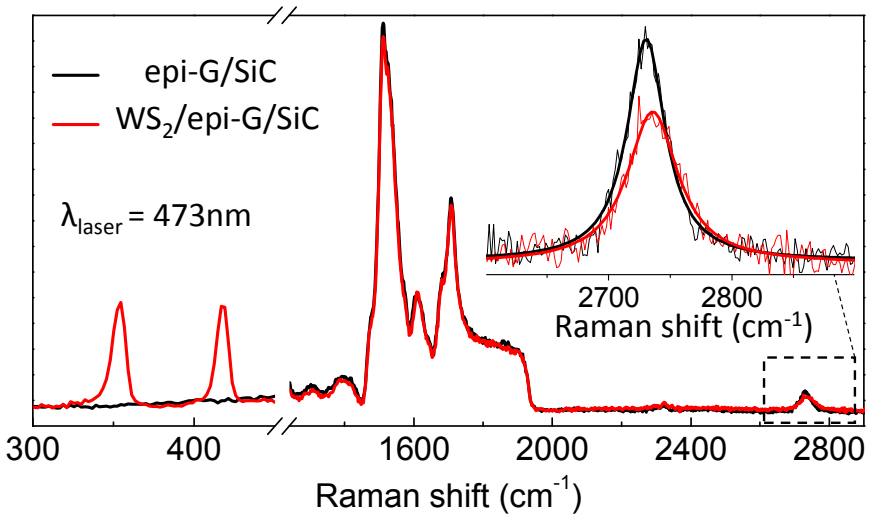

Fig. 3 Raman spectra of epi-G on SiC before and after WS_2 growth (10 min of deposition time). Inset shows a magnification of the 2D peak of epi-G.

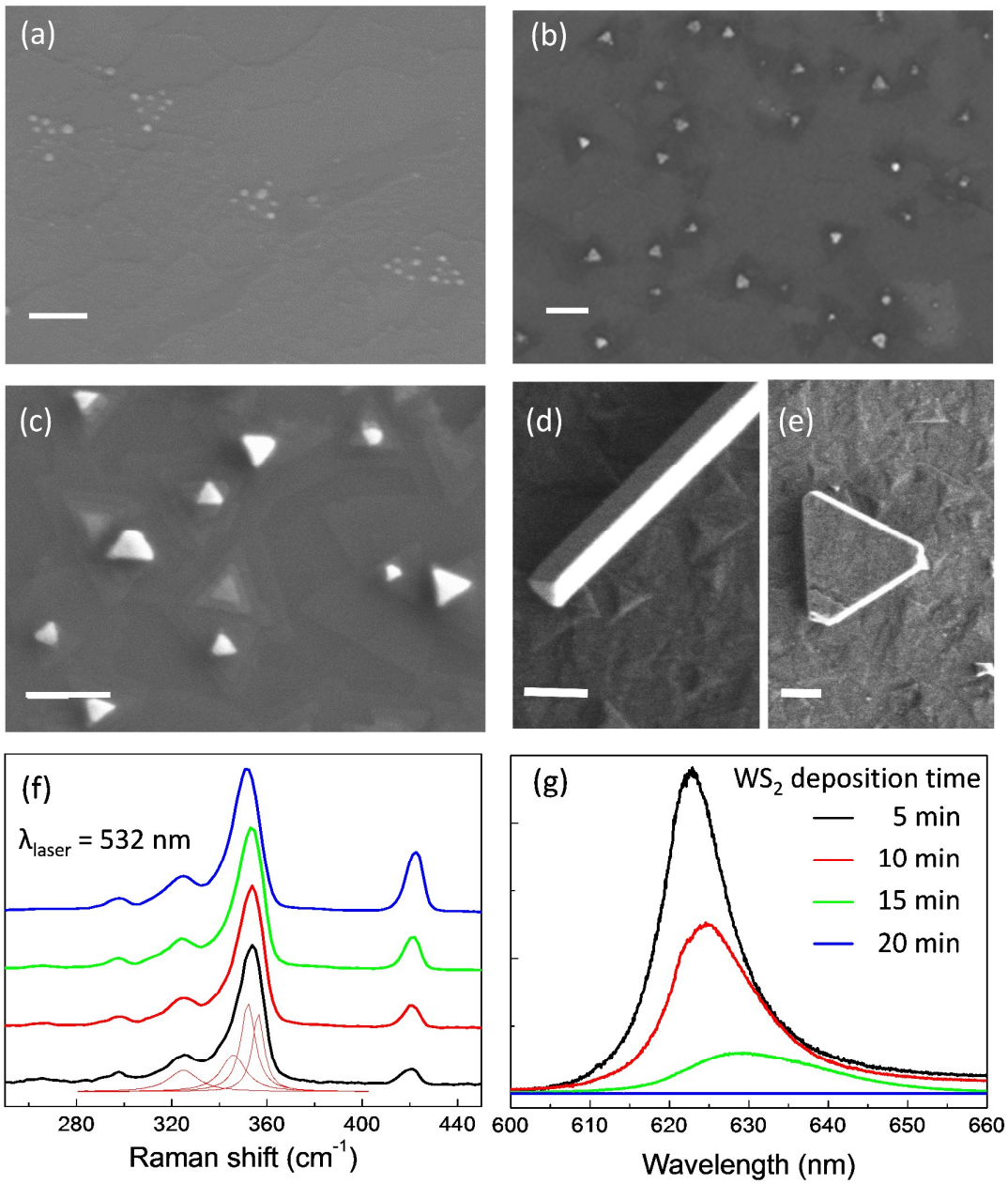

Fig. 4 (a-e) SEM images of WS_2 films grown on epi-G/SiC substrate for 5 (a), 10 (b), 15 (c), and 20 min (d, e) of deposition times (scale bars are 200 nm). (f) Raman and (g) photoluminescence spectra of WS_2 samples grown for different deposition times (legend in g). PL spectra are normalized to the intensity of the 2LA(M) Raman mode.

confirms the potential of van der Waals epitaxy in relaxing the interface between two materials.

The morphologies of WS_2 film grown on epi-G for deposition times of 5, 10, 15 and 20 min are shown on the SEM images reported in fig. 4 (a, b, c and d-e, respectively). For a deposition time of 5 min (fig. 4a), the sample still shows the terraces due to the miscut of the silicon carbide wafer which characterizes the morphology of an epi-G sample (see fig. S1 in electronic supplementary information, ESI). No substantial differences can be found in the morphology of the substrate before and after WS_2 growth except for the presence of nanometer sized clusters which are arranged in triangular geometries. These have been identified as sulfur condensed at the surface of triangular-shaped crystals of WS_2 whose presence is attested by both Raman and PL measurements (black spectra in figures 4f and 4g).[40]

For longer deposition times, the complete coalescence of WS_2 crystals into a continuous film occurs and the epi-G substrate loses its characteristic SiC terraced morphology (fig. 4b). Over this continuous film, we can notice isolated triangles supporting further WS_2 crystals which have nucleated in the proximity of their centers. Moreover, SEM images acquired by a second electron detector at the initial stage of WS_2 growth (see figure S2a and S2b) indicate that the formation of such

WS_2 new layers starts before the complete coverage of the substrate by a monolayer. Specifically, the growth starts with WS_2 monolayer with hundred nanometer size. For longer growing times (> 10 min), the continuous nucleation of new WS_2 layers gives rise to the formation of multilayered pyramids touching each other (fig. 4c) and evolving in a textured surface morphology (see background of fig. 4d and 4e). The last also promotes a totally different WS_2 growth mode leading to the formation of triangular quantum dots and nanowires (fig. 4d and 4e). Such transition to a quasi-unidimensional growth is indicative of a Stranski-Krastanov growth mode as reported also for the epitaxial growth of MoS_2 on mica.[41] The Stranski-Krastanov growth arises because strain energy in the deposited layers increases as the thickness increases, which is reflected by an increase in the interface energy between preformed and new WS_2 layer. Beyond a critical layer thickness, this leads to a switch in the growth mode that continues through the nucleation of new WS_2 layer rather than the lateral growth of preformed ones.

Raman and photoluminescence, PL, spectra provided by the different WS_2 morphologies are reported in figures 4f and 4g. When a WS_2 film is excited at 532 nm (almost in resonance with the B exciton transition), the Raman spectrum reveals a series of overtone and combination peaks not visible with a 473 nm laser source (see figure 3). The 2LA(M)−$2E^2_{2g}(\Gamma)$ mode appears at lower wavenumber (297 cm^{-1}), while the Raman feature around ≈350 cm^{-1} is the convolution of four peaks including the 2LA(M)−$E^2_{2g}(\Gamma)$, $E^1_{2g}(M)$, 2LA(M) and $E^1_{2g}(\Gamma)$ modes,[42] which are pointed at 325, 345, 352 and 356 cm^{-1}, respectively (values derived for the spectrum of the WS_2 sample grown with a deposition time of 5 min). Similar to the case of MoS_2, the Raman modes of WS_2 exhibit a thickness dependence. Upon increasing the WS_2 thickness from monolayer to bulk, several authors reported a gradual increase in the frequency difference between the A_{1g} mode and the $E^1_{2g}(\Gamma)$ (or 2LA(M)), which stiffens and softens, respectively.[10, 20, 39, 42-44] When a 532 nm laser source is used, the 2LA(M) results more prominent than the $E^1_{2g}(\Gamma)$ and, hence, the WS_2 thickness is typically correlated to its frequency. Despite the consistent differences between the morphologies of WS_2 films grown for 5 and 10 min (fig. 4a and b), their Raman spectra are almost identical (black and red lines in fig. 4f) with a 2LA(M) and A_{1g} modes at 352 and 420 cm^{-1}, respectively, and a frequency difference of 68 cm^{-1} that is consistent with the values previously reported for 2 layers of WS_2.[42, 43] For longer deposition times, the WS_2 Raman spectra present several changes. The increasing thickness is reflected by a gradual increase in intensity of the A_{1g} peak[43, 44] that also blue-shifts to 422 and 423 cm^{-1} for 15 and 20 min of deposition times, respectively, while the 2LA(M) modes are found at 352 and 350 cm^{-1}, respectively. Thus, we find values of frequency differences of 70 and 73 cm^{-1} which have previously been reported for 3-4 layers of WS_2 and WS_2 bulk, respectively.[43]

A stronger dependence is found between the morphologies of WS_2 films and their PL responses reported in fig. 4g. The samples present a single PL peak originating from the excitonic transition A whose intensity decreases with the increasing of growing times, up to the complete disappearance (as expected for WS_2 bulk). The isolated WS_2 triangles in fig. 4a present a PL peak located at 623 nm (1.99 eV) and a narrow fwhm of 27 meV. When the coalescence of WS_2 crystals in a continuous film occurs (growing time of 10 min, SEM image in fig. 4b), the sample shows a PL peak (red spectrum) slightly shifted toward longer wavelengths (625 nm at maximum) with an increased fwhm of 33 meV. The PL mapping of this sample (fig. S3 in supporting information) has also demonstrated an almost constant PL response over an area of 20 x 20 μm^2: PL wavelength at maximum of 625 ± 1 nm and a relative standard deviation below 20% on the PL intensity. For longer deposition time, the WS_2 pyramidal textures on fig. 4c and 4d-e present, respectively, a broad PL peak centered at 630 nm and the complete absence of PL signal. It is probable that the PL signal collected by the laser spot size (∼700 nm in diameter) is the contribution of different WS_2 domains. Anyway, the PL analysis demonstrates that this growth methodology can lead to WS_2 continuous film with homogeneous PL response as required by applications based on van der Waals heterostructures.

The use of CVD graphene supported on Si/SiO_2 as WS_2 substrate allows a better understanding of the sulfide growth mode. Since SEM analysis on SiO_2 substrate results in a better colour contrast for WS_2 rather than that observed on epi-G, the study of the WS_2 deposition also at the early stage of its growth is possible. SEM image in fig. 5a shows that the distribution density of WS_2 crystals after 5 min of growth is not homogeneous over the substrate surface. Specifically, the density of WS_2 crystals at graphene grain boundaries appears much higher than that inside the grains. This makes the polycrystalline structure of CVD graphene clearly visible. Such favoured WS_2 nucleation derives from the higher concentration of structural defects at graphene grain boundaries. Vacancies and Stone-Wales defects are formed between two coalesced graphene grains in order to accomplish their in plane misorientations.[45] These locally alter the chemical reactivity of graphene and, in our case, it results in a reduction of the WS_2 nucleation energy barrier.

A denser distribution of WS_2 crystals is also found in presence of graphene bilayer. The two specular regions in the center of fig. 5a correspond to bare SiO_2 (on the left side) and twisted bilayer graphene, TBG, (on the right side) which derive from the detachment and folding of the graphene film. The absence of graphene prevents the WS_2 growth on bare SiO_2. Conversely, WS_2 nucleation results strongly promoted on TBG as well as on Bernal-stacked bilayer graphene (BBG) islands.[46] These appear as darker grey regions inside graphene grains and derive from the nucleation and growth of a second graphene layer next to the substrate.[46]

Magnification in fig. 5b shows that isolated WS_2 triangles are not randomly oriented on the graphene surface. Inside a single graphene grain, we can distinguish equilateral triangles with only two different orientations related to each other by a rotation of 60°. Such not random distribution of WS_2 triangles is indicative of distinct crystallographic orientations between deposited TMDC and the substrate as previously demonstrated by diffraction techniques for the epitaxial

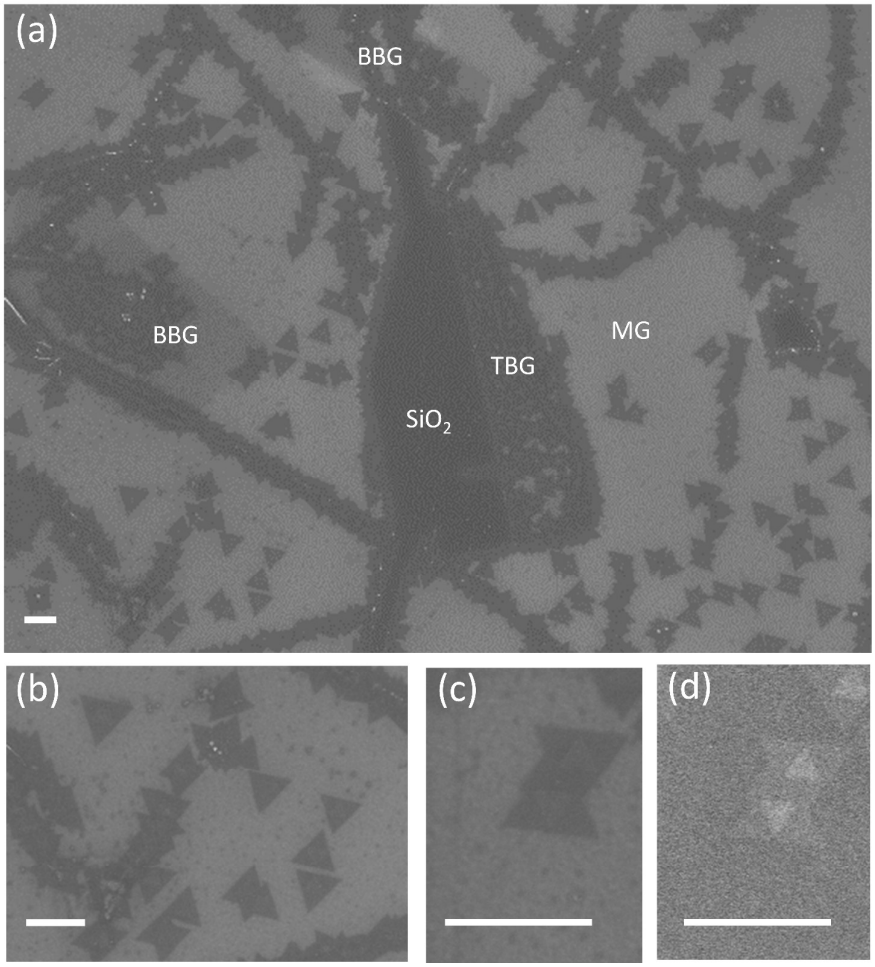

Fig. 5 SEM (a, b, and c) and SE2 (d) images of WS_2 grown on CVD graphene supported on SiO_2/Si substrate for 5 min of deposition time. The scale bars are 500 nm. Bare SiO_2 substrate, twisted bilayer graphene (TBG), and Bernal-stacked bilayer graphene (BBG) are indicated in (a).

growth of, MoS_2 on graphene[30] or sapphire,[47] WSe_2 on graphene,[29] and WS_2 on hBN.[27] Specifically, these works show how the orientation of TMDCs crystals with perfect triangular shape, as defined uniquely by a zigzag sulfur edge structure, can be univocally identified with their lattice orientation. Thus, we can attest for an epitaxial relation also for WS_2 on graphene and for the existence of substantial WS_2/graphene interactions which can affect the growth of WS_2 triangular crystals in order to find energetically favoured orientations.

Under continued growth, triangular crystals can merge to form a continuous WS_2 layer. However, the properties of the resulting WS_2 film will be strongly affected by its polycrystalline nature. The detrimental effects of grain boundaries on the optical and electrical properties of the film depend on the specific atomic structure of grain boundaries.[47-49] The last is strictly correlated to the relative in plane crystallographic orientations of two merging TMDCs crystals.[47-49] Previous studies on the large area growth of MoS_2 film have demonstrated that two TMDCs triangles sharing the same in plane orientation and, hence, crystalline orientation can join without the appearance of any grain boundaries.[47, 48] Thus, the growth of WS_2 triangles with only two distinctive in plane orientations offers a great potential for the deposition of polycrystalline large area film with reduced density of grain boundaries. Conversely, if TMDCs merging triangles are misaligned, the strong directional dependence of surface energies of their edges[48] can result into strongly faceted grain boundaries ("tilted" grain boundaries) or into overlapping regions.[47-49] Indeed, TMDCs triangles with a relative in-plane rotation of 60° (as shown in figure 5b) provide the perfect alignment of their zigzag sulfur edges which results into a specific grain boundary atomic structure named as "mirror twin".[47, 48] In contrast to "tilted" grain boundaries, the "mirror twin" ones have been experimentally demonstrated not to degrade the electrical properties of a polycrystalline TMDC film.[47, 48] However, the possibility of depositing WS_2 continuous film with reduced density of grain boundaries and with the favoured formation of "mirror twin" boundaries is confined to a single graphene grain. For larger areas, the polycrystalline nature of the substrate will be also reflected in the WS_2 film.

The SEM image reported in fig. 5c shows a detail of the edges alignment between two tilted merging triangles. The same image has been acquired also by using a secondary electron,

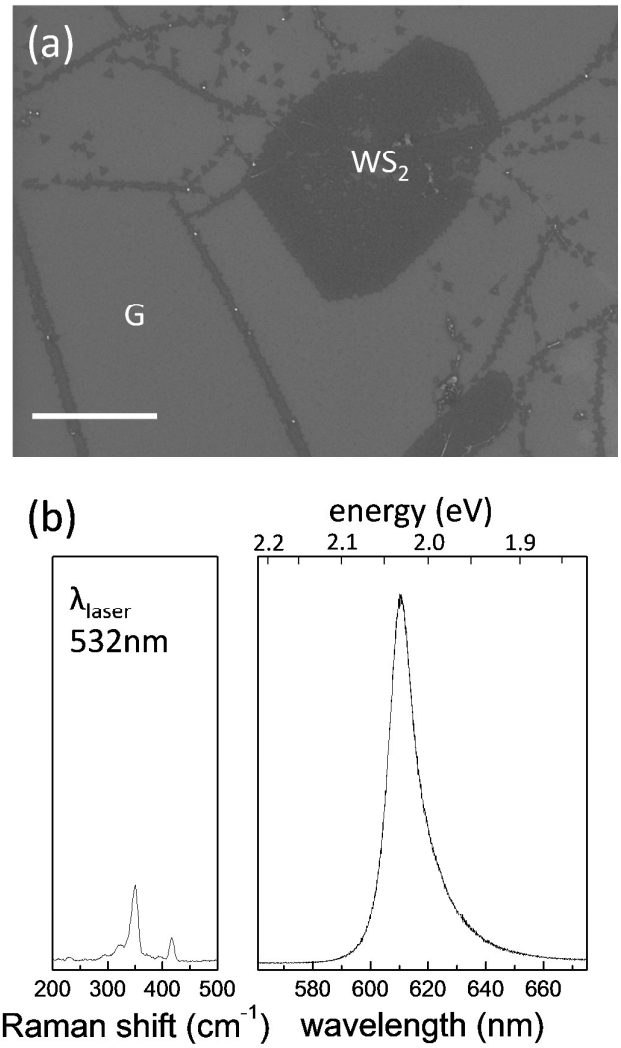

Fig. 6 (a) SEM image of the localized growth of WS_2 (deposition time of 2 min) on a bilayer graphene island. Scale bar is 2 µm. (b) Raman and PL spectra of WS_2 film grown on BBG. The graphs have the same intensity scale.

SE2, detector (fig. 5d) since it provides a sharper thickness-dependent contrast for 2D materials on insulating substrates.[50] The image attests for the absence of an overlapped junction between merging WS_2 triangles and highlights the presence of supplementary WS_2 triangular layers already formed over them. Thus, when WS_2 nuclei are formed, their lateral growth is in competition with the growth of new WS_2 layers starting from the same nucleation seeds. Such growth mode is consistent with a Volmer–Weber one and leads to the formation of multilayered WS_2 islands rather than a continuous film with uniform thickness (defined layers number) as desired for applications in devices based on van deer Waals heterostructures. Considering only thermodynamic criterions, the Volmer-Weber growth is indicative of a weaker interaction between WS_2 and graphene than between WS_2 layers. In terms of surface energies (y), the islands growth mode occurs when $y_{WS2}>y_{graphene}+y^*$, where y* is the graphene/WS_2 interface energy. The main issue relies on the extremely low surface energy of monolayer CVD graphene ($y_{graphene}\approx 70$ mJ/m^2) in comparison to the WS_2 one ($y_{WS2} \approx 260$ mJ/m^2).[51] This limits the WS_2 nucleation as well as the attachment of sulfur and tungsten adatoms to the edges of WS_2 monolayer.

Conversely, the favoured WS_2 nucleation on TBG and BBG (fig. 4a) derives from the (25%) higher surface energy value of bilayer graphene compared to that of monolayer one.[52] Fig. 6 demonstrates that the high density of nucleation sites on BBG can provide the localized deposition of a WS_2 film on the bilayer graphene island whit almost no sulfide deposition inside monolayer graphene grains. The high structural quality and few layer nature of WS_2 film grown on BBG is attested by a frequency difference between 2LA(M) and $A_{1g}(\Gamma)$ Raman modes of 66 cm^{-1} and a PL peak with a maximum at 610 nm (2.03 eV) and an intensity five times higher than the Raman features at ≈ 350 cm^{-1}.

Conclusions

We have reported the successful van der Waals epitaxy of WS_2 on epi-G and CVD-G by direct CVD growth with $W(CO)_6$ and elemental sulfur as precursors. The Raman analysis on WS_2/epi- G has highlighted the absence of strain at the heterostucture interface as well as the absence of graphene defects induced by the deposition process. The PL analysis has demonstrated that this synthetic route can provide continuous WS_2 films with homogeneous PL response. Moreover, SEM analysis has shown the occurrence of an epitaxial growth leading to specific in plane orientations which provides a great potential for the growth of large area continuous film. Finally, the possibility of tuning the WS_2 growth dynamic and localizing WS_2 deposition by tailoring the graphene surface energy has been demonstrated. The proposed growth methodology opens the way towards the direct bottom up fabrication of a huge variety of TMDCs/graphene devices that are based on van der Waals heterostructures integrating 2D materials.

Experimental

The epi-G substrates were fabricated by thermal annealing of hydrogen-plasma cleaned 6H-SiC substrates at 1500°C for 2 min at 10^{-8} mbar. CVD-G was grown on 25 µm thick copper foils at 1000 °C using CH_4/H_2 as precursors. The prepared graphene was then transferred onto 300 nm SiO_2/Si substrates by using a thermal release tape and a water solution of ammonium persulfate (0.1 M) as copper etchant. The methodology for the growth of WS_2 is reported in the main text.

WS_2 Raman and PL spectra were collected using a LabRAM HR Horiba-JobinYvon spectrometer with a 473 and 532 nm excitation laser sources, and a 100X objective.

Ellipsometric spectra were acquired using a phase-modulated spectroscopic ellipsometer (UVISEL, Horiba JobinYvon) in the 1.5–3.25 eV spectral range with 0.01 eV resolution.

The sample morphology was studied through field emission scanning electron microscopy (FE-SEM) observations, using a Carl Zeiss Sigma microscope, equipped with a high resolution FE-SEM Gemini electron column, an in-lens detector (SE) placed inside the electron column, and an external Everhart-Thornley detector (SE2) placed outside the column. A primary electron beam acceleration voltage ranging between 1 and 5 kV and a working distance of around 3mm were employed.

Acknowledgements

The authors acknowledge funding from the National Laboratory Sens&Micro LAB Project (POFESR 2007–2013, code number 15) funded by Apulia Region. The authors wish to acknowledge F. Marzo for FE-SEM observations.

References

1 Q. H. Wang, K. Kalantar-Zadeh, A. J. Kis, N. Coleman, M. S. Strano, Nature Nanotechnology, 2012, **7**, 699.
2 M. Xu, T. Lian, M. Shi, H. Chen, Chemical Review, 2013, **113**, 3766.
3 A. K. Geim, I. V. Grigorieva, Nature, 2013, **499**, 419.
4 M. Bosi, RSC Adv., 2015, **5**, 75500.
5 A. Splendiani, L. Sun, Y. Zhang, T. Li, J. Kim, C. Chim, G. Galli, F. Wang, Nano Letters, 2010, **10**, 1271.
6 K. F. Mak, C. Lee, J. Hone, J. Shan, T. F. Heinz, Phys. Rev. Lett., 2010, **105**, 136805.
7 W. Zhao, R. M. Ribeiro, M. Toh, A. Carvalho, C. Kloc, A. H. Castro Neto, G. Eda, Nano Letters 2013, **13**, 5627.
8 Y. Zhang, T. Chang, B. Zhou, Y. Cui, H. Yan, Z. Liu, F. Schmitt, J. Lee, R. Moore, Y. Chen, H. Lin, H. Jeng, S. Mo, Z. Hussain, A. Bansil, Z. Shen, Nature Nanotech., 2014, **9**, 111.
9 W. Zhao, Z. Ghorannevis, L. Chu, M. Toh, C. Kloc, P. Tan, G. Eda, ACS Nano, 2013, **7**, 791.
10 H. R. Gutierrez, N. Perea-Lopez, A. L. Elías, A. Berkdemir, B. Wang, R. Liv, F. Lopez-Urías, V. H. Crespi, H. Terrones, M. Terrones, Nano Letters, 2013, **13**, 3447.
11 V. Kertinin, Y. Cao, J. S. Tu, G. L. Yu, R. Jalil, K. S. Novoselov, S. J. Haigh, A. Gholinia, A. Mishchenko, M. Lozada, et al, Nano Letters 2014, **14**, 3270.
12 J. Y. Tan, A. Avsar, J. Balakrishnan, G. K. W. Koon, T. Taychatanapat, E. C. T. O'Farrell, K. Watanabe, T. Taniguchi, G. Eda, A. H. Castro Neto, B. Özyilmaz, Appl. Phys. Lett., 2014, **104**, 183504.
13 S. Larentis, J. R. Tolsma, B. Fallahazad, D. C. Dillen, K. Kim, A. H. MacDonald, E. Tutuc, Nano Letters, 2014, **14**, 2039.
14 G. Fiori, F. Bonaccorso, G. Iannaccone, T. Palacios, D. Neumaier, A. Seabaugh, S. K. Banerjee, L. Colombo, Nature Nanotech., 2014, **9**, 768.
15 J. V. Lauritsen, J. Kibsgaard, S. Helveg, H. Topsoe, B. S. Clausen, E. Lagsgaard, F. Besenbacher, Nature Nanotechnol., 2007, **2**, 53.
16 S. Helveg, J. V. Lauritsen, E. Lægsgaard, I. Stensgaard, J. K. Nørskov, B. S. Clausen, H. Topsøe, F. Besenbacher, Phys. Rev. Lett., 2000, **84**, 951.
17 C. M. Orofeo, S. Suzuki, Y. Sekine, H. Hibino, Appl. Phys. Lett., 2014, **105**, 083112.
18 Y. H. Lee, X. Q. Zhang, W. Zhang, M. T. Chang, C. T. Lin, K. D. Chang, Y. C. Yu, J. T. W. Wang, C. S. Chang, L. J. Li, T. Lin, Advanced Materials, 2012, **24**, 2320.
19 K. K. Liu, W. Zhang, Y. H. Lee, Y. C. Lin, M. T. Chang, C. Y. Su, C. S. Chang, H. Shi, Y. Li, H. Zhang, C. S. Lai, L. J. Li, Nano Letters, 2012, **12**, 1538.
20 Y. Zhang, Q. Ji, J. Ju, H. Yuan, J. Shi, T. Gao, D. Ma, M. Liu, Y. Chen, X. Song, H. Y. Hwang, Y. Cu, Z. Liu, ACS Nano, 2013, **7**, 8963.
21 C. Cong, J. Shang, X. Wu, B. Cao, N. Peimyoo, C. Qiu, L. Sun, T. Yu, Adv. Optical Mater., 2014, **2**, 131.
22 J. K. Huang, J. Pu, C. L. Hsu, M. H. Chiu, Z. Y. Juang, Y. H. Chang, W. H. Chang, Y. Iwasa, T. Takenobu, L. J. Li, ACS Nano, 2014, **8**, 923.
23 Y. H. Lee, L. Yu, H. Wang, W. Fang, X. Ling, Y. Shi, C. T. Lin, J. K. Huang, M. T. Chang, C. S. Chang, M. Dresselhaus, T, Palacios, L. J. Li, J. Kong, Nano Lett., 2013, **13**, 1852.
24 N. Perea-Lopez, A. L. Elıas, A. Berkdemir, A. Castro-Beltran, H. R. Gutierrez, S. Feng, R. Lv, T. Hayashi, F. Lopez-Urıas, S. Ghosh, B. Muchharla, S. Talapatra, H. Terrones, M. Terrones, Adv. Funct. Mater., 2013, **23**, 5511.
25 X. Duan, C. Wang, J. C. Shaw, R. Cheng, Y. Chen, H. Li, X. Wu, Y. Tang, Q. Zhang, A. Pan, J. Jiang, R. Yu, Y. Huang, X. Duan, Nature Nanotech., 2014, **9**, 1024.
26 Y. Fan, G. Hao, S. Luo, X. Qi, H. Li, L. Ren, J. Zhong, AIP Advances, 2014, **4**, 057105.
27 M. Okada, T. Sawazaki, K. Watanabe, T. Taniguch, H. Hibino, H. Shinohara, R. Kitaura, ACS Nano, 2014, **8**, 8273.
28 Y. Shi, W. Zho, A. Y. Lu, W. Fang, Y. H. Lee, A. L. Hsu, S. M. Kim, H. Y. Yang, L. J. Li, J. C. Idrobo, J. Kong, Nano Lett., 2012, **12**, 2784.
29 A. Azizi, S. Eichfeld, G. Geschwind, K. Zhang, B. Jiang, D. Mukherjee, L. Hossain, A. F. Piasecki, B. Kabius, J. A. Robinson, N. Alem, ACS Nano, 2015, **9**, 4882.
30 H. Ago, H. Endo, P. Solís-Fernández, R. Takizawa, Y. Ohta, Y. Fujita, K. Yamamoto, M. Tsuji, ACS Appl. Mater. Interfaces, 2015, **7**, 5265.
31 Y. Lin, N. Lu, N. Perea-Lopez, J. Li, Z. Lin, X. Peng, C. H. Lee, C. Sun,L. Calderin, P. N. Browning, M. S. Bresnehan, M. J. Kim, T. S. Mayer,M. Terrones, J. A. Robinson, ACS Nano, **8**, 3715
32 K. Zhou, F. Withers, Y. Cao, S. Hu, G. Yu, C. Casiraghi, ACS Nano, 2014, **8**, 9914.
33 Y. Kobayashi, S. Sasaki, S. Mori, H. Hibino, Z. Liu, Z. Watanabe, T. Taniguchi, K. Suenaga,Y. Maniwa, Y. Miyata, ACS Nano, 2015, **9**, 4056.
34 A. Koma, Thin Solid Films, 1992, **216**, 72.
35 S. M. Eichfeld, L. Hossain, Y. Lin, A. F. Piasecki, B. Kupp, A. G. Birdwell, R. A. Burke, N. Lu, X. Peng, J. Li, A. Azcatl, S. McDonnell, R. M. Wallace, M. J. Kim, T. S. Mayer, J. M. Redwing, J. A. Robinson, ACS Nano, 2015, **9,** 2080.
36 A. R. Beal, J. C. Knights, W. Y. Liang, J. Phys. C: Solid State Phys., 1972, **5**, 3540.
37 Y. Li, A. Chernikov, X. Zhang, A. Rigosi, H. M. Hill, A. M. van der Zande, D. A. Chenet, E. Shih, J. Hone, T. F. Heinz, Physical review B, 2014, **90**, 205422.
38 D. S. Lee, C. Riedl, B. Krauss, K. von Klitzing, U. Starke, J. H. Smet, Nano Lett., 2008, **8**, 12, 4320.
39 W. Zhao, Z. Ghorannevis, K. K. Amara, J. R. Pang, M. Toh, X. Zhang, C. Kloc, P. H. Tane, G. Eda, Nanoscale, 2013, **5**, 9677.
40 Q. Ji, Y. Zhang, T. Gao, Y. Zhang, D. Ma, M. Liu, Y. Chen, X. Qiao, P. Tan, M. Kan, J. Feng, Q. Sun, Z. Liu, Nano Lett. 2013, **13**, 3870.
41 J. Ouerfelli, J. C. Bernède, A. Khelil, J. Pouzet, Applied Surface Science, 1997, **120**, 1.
42 N. Peimyoo, J. Shang, W. Yang, Y. Wang, C. Cong, T. Yu, Nano Res., 2015, **8**, 1210.
43 F. Withers, T. H. Bointon, D. C. Hudson, M. F. Craciun, S. Russo, Sci. Rep., 2014, **4**, 4967.
44 A. Berkdemir, H. R. Gutièrrez, A. R. Botello-Mèndez, N. Perea-Lòpez, A. L. Elìas, C. Chia, B. Wang, V. H. Crespi, F. Lòpez-Urìas, J. Charlier, H. Terrones, M. Terrones, Sci. Rep., 2014, **3**, 1755.
45 J. Wu, Y. Wei, Journal of the Mechanics and Physics of Solids, 2013, **61**, 1421.

46 S. Nie, W. Wu, S. Xing, Q. Yu, J. Bao, S. Pei, K. F. McCarty, New Journal of Physics, 2012, **14**, 093028.
47 D. Dumcenco, D. Ovchinnikov, K. Marinov, P. Lazi, M. Gibertini, N. Marzari, O. L. Sanchez, Y. Kung, D. Krasnozhon, M. Chen, S. Bertolazzi, P. Gillet, A. Fontcuberta i Morral, A. Radenovic, A. Kis, ACS Nano, 2015, **9**, 4611.
48 A. M. van der Zande, P. Y. Huang, D. A. Chenet, T. C. Berkelbach, Y. You, G. Lee, T. F. Heinz, D. R. Reichman D. A. Muller, J. C. Hone, Nature Materials, 2013, **12**, 554.
49 S. Najmaei, Z. Liu, W. Zhou, X. Zou, G. Shi, S. Lei, B. I. Yakobson, J. Idrobo, P. M. Ajayan, J. Lou, Nature Materials, 2013, **12**, 754.
50 V. Kochat, A. N. Pal, E. S. Sneha, B. S. Arjun, A. Gairola, S. A. Shivashankar, S. Raghavan, A. Ghosh, Journal of Applied Physics, 2011, **110**, 014315.
51 J. N. Coleman, M. Lotya, O. O'Neill, S. D. Bergin, P. J. King, U. Khan, K. Young, A. Gaucher, S. De, R. J. Smith, et al, Science, 2011, **331**, 568.
52 C. J. Shih, M. S. Strano, D. Blankschtein, Nature Materials, 2013, **12**, 866.

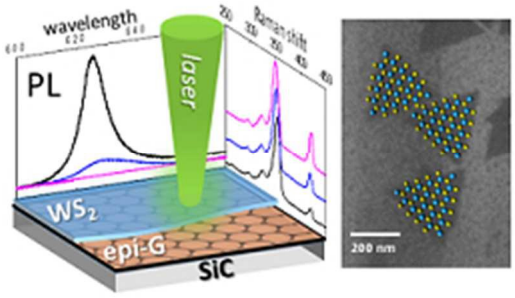

Direct epitaxial growth of WS2 isolated crystals and WS2 continuous films providing homogeneous and narrow PL peak onto epitaxial- and CVD-graphene
69x41mm (96 x 96 DPI)